Mining, Metallurgy & Exploration (2022) 39:1017–1026
https://doi.org/10.1007/s42461-022-00579-z

Stress Redistribution in a Longwall Yield Pillar — a Comparison between Active Seismic Tomography and Theory

Erik C. Westman[1] · Jessica M. Wempen[2] · Dallan J. Coons[2] · Michael K. McCarter[2] · William G. Pariseau[2]

Received: 2 June 2021 / Accepted: 21 February 2022 / Published online: 18 March 2022

Abstract
Gate road yield pillars are subject to increases in stress as the longwall face advances through a panel. Safe, efficient underground mining is dependent upon proper pillar sizing. Theoretical models of pillar loading are well accepted, and geotechnical measurements, including convergence monitoring, have provided important information about stress levels and distributions within pillars. Numerical modeling has developed as a method which complements empirical and theoretical pillar behavior concepts, and allows prediction of the behavior of various pillar sizes under changing conditions. Seismic tomography has seen fairly limited application in the mining industry, but has potential to be a valuable method to further improve understanding of coal pillar performance under changing loading conditions. This research presents a case study from a longwall mine in the western USA. A two-entry gate road yield pillar in the headgate of the mine was instrumented with seismometers and convergence monitoring stations, and was monitored over a period of about 6 months as the longwall face approached the pillar. In this paper, the stress distribution imaged using seismic tomography is compared to the stress distribution expected from theoretical models, geotechnical measurements, and numerical models. The tomography results generally agree with those proposed by theory, convergence measurements, and numerical modeling results. The agreement of the methods provides validation for the theorized stress redistribution, and this study provides further evidence that tomography can indicate the redistribution of induced stress within a mined rockmass and is another tool available to ensure that mining is conducted safely and efficiently.

Keywords Longwall mining · Seismic tomography · Coal · Ground control

1 Introduction

Safe, efficient underground mining is dependent upon proper pillar sizing. Pillar sizing is typically based on a combination of observation of prior behavior, point measurements, theory, and numerical modeling. The actual stress redistribution within a pillar, while assumed for many years, has rarely been imaged. Such imaging can help confirm whether or not theoretical and numerical modeling methods agree with actual conditions within a pillar.

Pillars must be sized large enough to provide safe support for the underground operations, but also to allow for optimal recovery of a resource. Typically, pillars are sized according to existing design criteria and prior performance at the current mine or a nearby mine. Pillar performance can be predicted with numerical modeling and monitored with geotechnical instrumentation, but there are very few published accounts confirming actual stress redistributions within pillars by imaging. In addition to confirming actual stress redistribution, imaging could support a more complete understanding actual pillar behavior and lead to more optimal structural design.

A case study from a longwall mine in the western USA provided an opportunity to compare the imaged stress distribution with that expected from theoretical models, geotechnical measurements, and numerical models. Seismic traveltime data were used to image P-wave velocity changes, indicating induced stress changes, in a yield pillar at a longwall mine as the longwall face drew nearer to the pillar. Based on previously published results using theory, point measurements, and numerical modeling, we hypothesize that

✉ Erik C. Westman
ewestman@vt.edu

[1] Department of Mining and Minerals Engineering, Virginia Tech, Blacksburg, VA, USA

[2] Department of Mining Engineering, University of Utah, Salt Lake City, UT, USA

the induced stress within the pillar increases as the longwall face draws nearer, and ultimately, the stress decreases due to failure within the pillar. Using data from a yield pillar, the objective of this study is to compare both the expected stress change based on theory and estimated from numerical models to the velocity change observed with active seismic tomography.

2 Background

Excellent work has been conducted over the past 50 years in the field of coal pillar design, initially with empirical and theoretical models, then with measurements, and more recently with numerical modeling. Additional work has been conducted for hard rock pillar design; however, this review focuses on coal pillar loading and load distribution. We also recognize that outstanding research on stress redistribution within longwall pillars has been conducted globally; however, we focus on prior research in seam conditions in the USA that are most similar to the current study.

Initial efforts to quantify a safe pillar design proposed a pillar strength that is a function of the coal seam strength and the pillar width and height; equations were developed by several researchers [1–4]. Following these efforts, Wilson [5, 6] proposed that the stress redistribution within a coal pillar, and hence the pillar strength, was influenced by a confined core which had a much greater strength than the perimeter of the pillar. The concept of a confined core within a pillar and the acknowledgement that the loading conditions of pillars change as a function of development and nearby production were accepted and further developed.

Review of coal pillar design indicated potential shapes for the stress distribution within pillars by showing that the stress distribution assumed in the Mark-Bieniawski pillar design formula is a pyramid for square pillars and a rectangular, elongated pyramid (with a linear apex) for rectangular pillars [7]. The load is a maximum in the center of a pillar (at a point for a square pillar and along a line for a rectangular pillar) and a minimum at pillar ribs. The ultimate strength of the pillar is governed by the strength of the core. Prior to this demonstration, Wagner [8, 9] presented a model of stress redistribution within a pillar that has been broadly accepted: failure occurs starting at the perimeter of a pillar and gradually progresses inwards toward a confined core which will fail if the stress exceeds the ultimate strength of the pillar.

Like theoretical models, geotechnical measurements have also provided much information about the stress levels and distributions within coal pillars. Instrumentation for geotechnical monitoring of pillar stress has typically included borehole pressure cells, hollow-inclusion cells, and vibrating wire stress meters. Geotechnical measurements have confirmed the development of a confined core within a pillar as the load upon the pillar increases. One example from a longwall mine in the western USA showed overburden stresses of 8 MPa, and stresses in a yield pillar under side abutment loading of 15–20 MPa [10].

Over the past 30 years, numerical modeling has developed as a method which complements the empirical and theoretical pillar behavior concepts. Esterhuizen et al. [11] compared stress distribution from Mark's empirical equation [12] to that obtained with numerical modeling and found that there was generally a good agreement between the empirical and numerical approaches. In their case study of a longwall mine in the eastern United States, the background stress level was approximately 5 MPa and the peak stress in a chain pillar near the active longwall face was 27 MPa in the numerical modeling results and 24 MPa from Mark's empirical equation. As a method for providing information about the stress within coal pillars, numerical modeling allows prediction of the behavior of various pillar sizes under changing conditions, and it has the ability to extend the geotechnical behavior of a pillar throughout a pillar's entire volume, which can complement the information provided by point-location geotechnical measurements.

Although it has seen limited application, seismic tomography has potential to be a valuable method to further improve understanding of the performance of coal pillars under changing loading conditions. Seismic tomography allows for the imaging of the interior of a body by analysis of energy that has propagated from one boundary to another. Computed tomography (CT) has grown from initial implementation in the late 1960s [13, 14] to a standardized tool in the medical field, and this method has been previously used for examining stress redistribution in longwall pillars [15, 16]. Tomography offers an independent method to which numerical models can be compared, and while numerical modeling is valuable and point-location geotechnical measurements are critical, tomography provides a means to understand stress redistribution throughout the entire volume of the pillar. This paper presents a comparison between measurements, modeling, and inferred stress from active seismic tomography in a yield pillar in a longwall coal mine, with stress increasing on the pillar over time due to increasing proximity of the longwall face.

3 Methods

The study presented in this paper was conducted at a longwall mine in the western USA under approximately 400 m of overburden cover. The yield pillar that was studied was located approximately 125 m from the recovery room of longwall panel that was 260 m wide and 1800 m long. The yield pillar was approximately 55 m long and 11 m wide and was in the two-entry headgate. The panel was surrounded by

unmined coal. The seam thickness averaged 3 m and there was a shale parting within the coal seam of approximately 0.3 m thickness at 1.5-m height above the floor. The immediate roof and floor were composed of shaly sandstone with occasional mudstone lenses. The current study is differentiated from prior studies, e.g. [15, 16], in that it collected seismic data transmitted through the interior of a pillar, rather than the roof or floor, and it analyzed a yield pillar rather than an abutment pillar.

Figure 1 shows geophone locations and the locations where convergence was monitored. Six uniaxial and two triaxial geophones were installed in the study pillar. Drillhole collar locations were selected to provide unobstructed access to the rib and to maintain approximately equal spacing between the sensors on the travelway and beltway sides of the pillar. The uniaxial geophones had a 2.54-cm diameter, and were installed in holes drilled into the pillar with a 3.5-cm diameter bit. The triaxial geophones had a 5.08-cm diameter, and were installed in holes drilled into the pillar with a 7.6-cm diameter coring bit. The holes were drilled from the entries into the ribs of the pillar to an average depth of 2.1 m at a height of about 1.2 m from the base of the pillar, and were drilled at a slight incline, about 12° from horizontal and about orthogonally to the travelway and beltway ribs. All of the geophones were mounted in the holes using either epoxy or grout and were connected to a seismic recording station located in intake air in the cross-cut immediately outby the instrumented pillar.

Active seismic sources were generated by striking the pillar with a battering ram. The ram was constructed with an interior movable mass to produce a "dead blow" to eliminate, as far as possible, repeated signal from a bounce back or double strike on the pillar. During active source generation, the pillar was struck three times, consecutively, below the geophone hole collars, so the travel times could be averaged and the events could be uniquely distinguished as active sources, and the sources would not be possibly confused with mining-induced seismicity (MIS). Each blow of the ram at a given site produced three very similar wave forms at each geophone receiver; however, the characteristics of the arriving waveforms varied at each geophone receiver. Active source signals, generated by striking, were recorded regularly over the course of about four months, September through December 2017. Passive source signals, from MIS and equipment noise, were recorded continually over the same period. During the study, the longwall face advanced approximately 940 m toward the pillar. Active source data from four dates, October 18, November 18, December 18, and December 27, 2017, were selected for seismic analysis as part of this study.

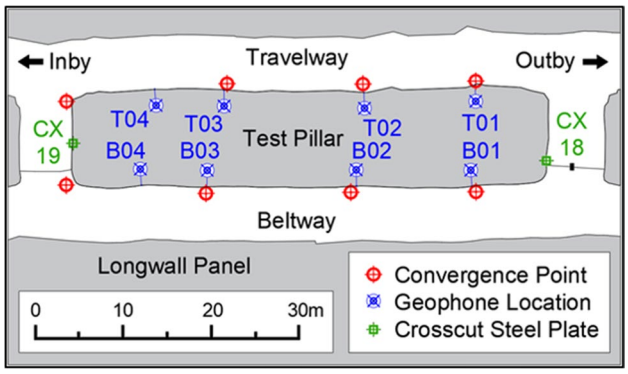

Fig. 1 Locations of geophones and convergence stations

The first motion of the direct waves of each active source were picked manually using Seismic Analysis Code [17, 18] to define the arrival time of each event at each geophone. For each active source event, travel times through the pillar were calculated by differencing the arrival times at each geophone from the arrival times at the geophone nearest the source events. Because there were three strikes generated consecutively at each source, three travel times for each assumed raypath were calculated; the travel times were averaged. Velocities were estimated from the assumed raypath distance and the travel time. Some unreasonably high velocities, higher than 3600 m/s, were encountered. These high velocities are most likely due to errors in the pick times, and were removed from the analysis.

The velocity distribution within the pillar was calculated for each of the four dates using seismic tomography to evaluate how the stress redistribution within the pillar estimated by tomography compared to theoretical and numerical results. Reliable results from tomography calculations depend on several factors including the quality of the input data, the method used for raytracing, the raypath coverage through the volume of interest, and the method used for inverting for the velocity distribution.

3.1 Data Quality

The input data quality is demonstrated by Fig. 2, which shows the distance between source and receiver versus the travel time of the seismic P-wave for each of the dates studied. Results of least squares regression for each date are summarized in Table 1. Regression were fixed with an intercept of 0 s. The correlation between distance and travel time, quantified by r^2, varies from 0.70 to 0.91; based on prior experience, these r^2 values indicate good data quality. Because the surveys were conducted through an intact pillar, it was expected that the distance and travel time would be highly correlated; if the survey had included voids, such as mine openings, then the correlation would be expected to be lower. The average P-wave velocity through the pillar for each of the time periods ranged from 2404 to 2899 m/s,

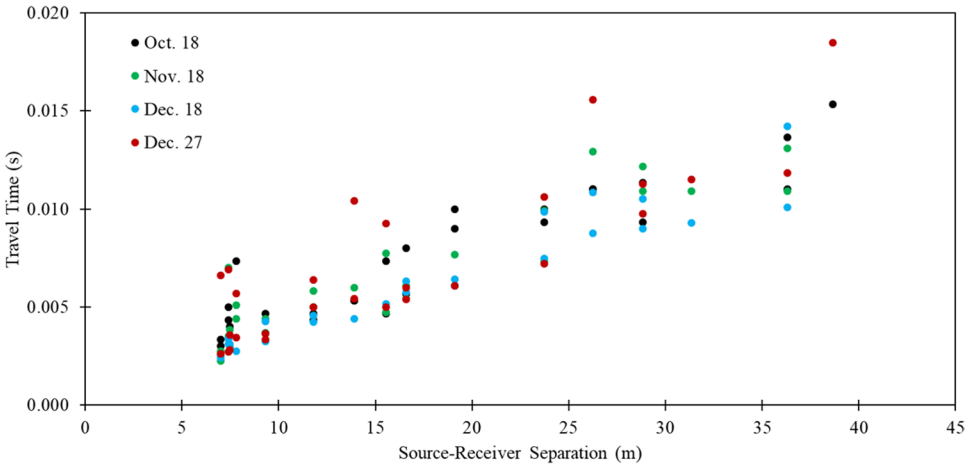

Fig. 2 Distance versus travel time for four time periods, adapted from [19]

Table 1 Distance versus travel time regressions, correlations, and average velocities

Date	Least Squares Regression (y = mx + b)		r^2	Average Velocity (m/s)
	b (s)	m (s/m)		
Oct. 18	0	0.000395	0.82	2532
Nov. 18	0	0.000382	0.78	2618
Dec. 18	0	0.000345	0.91	2899
Dec. 27	0	0.000416	0.70	2404

with the velocity increasing from the first to third surveys, then decreasing from the third to fourth.

3.2 Raytracing

When seismic waves travel through media of varying modulus, the waves refract such that the first-arriving energy has followed a curved raypath. Because the velocity distribution within the pillar is assumed to be non-uniform it is necessary to approximate the curved raypath in order to achieve the best tomographic results possible. A Matlab-based implementation of the Fast Marching Method was used to determine the paths of the P-waves through the pillar [19, 20]. This method was developed by Sethian and provides an efficient and accurate solution to the Eikonal equation [21].

3.3 Inversion and Raypath Coverage

Inversion of the velocity distribution was conducted using the Simultaneous Iterative Reconstruction Technique (SIRT). With tomography, the volume of interest is divided into discrete units (termed 'voxels'), and the portion of the curved raypath within each of the voxels that it traverses is catalogued and summed for all raypaths that travel through each voxel. A correction factor based on the difference between the calculated and measured travel times is then applied as a function of the length of the ray through a voxel compared to the total ray length.

The selection of the optimal voxel size depends on the number of rays used to image the volume of interest, and it must balance resolution versus accuracy of the results. More accurate results are obtained by using relatively more rays per voxel, and hence a larger voxel size; however, with larger voxel sizes, the resolution of the results is diminished. Rawlinson [22] provides a description of several methods that use synthetic travel times to ensure that the results are adequately supported by the input data. The checkerboard method employs synthetic arrival times calculated for rays that travel through alternating voxels of high and low velocity; the synthetic arrival times are then inverted and the reliability of the output is determined by the ability to regenerate the input checkerboard pattern. Rawlinson, however, proposes using more widely-spaced high- and low-velocity voxels ("spikes") for generating the synthetic arrival times, arguing that this allows the user to more readily determine where smearing of the results occurs due to poor raypath geometry.

For each day that data were collected, there were about 15 raypaths through the interior of the pillar plus an additional 30 or so along the ribs, for a typical total of about 45 raypaths for each of the four days that data were analyzed. The typical frequency of the P-wave arrivals was 1000 Hz, and hence a typical wavelength is 2.5 m at an average velocity of 2500 m/s.

Best tomography results are obtained when multiple rays pass through a voxel and from multiple angles. Because of the relatively few rays available for the current study, an appropriate voxel size was determined by examining the number of rays per voxel within the pillar, for varying voxel sizes. Figure 3 shows voxel spacings ranging from 0.83 to 5 m, and also voxels that have at least three rays passing through them (the legend for each plot shows the number of

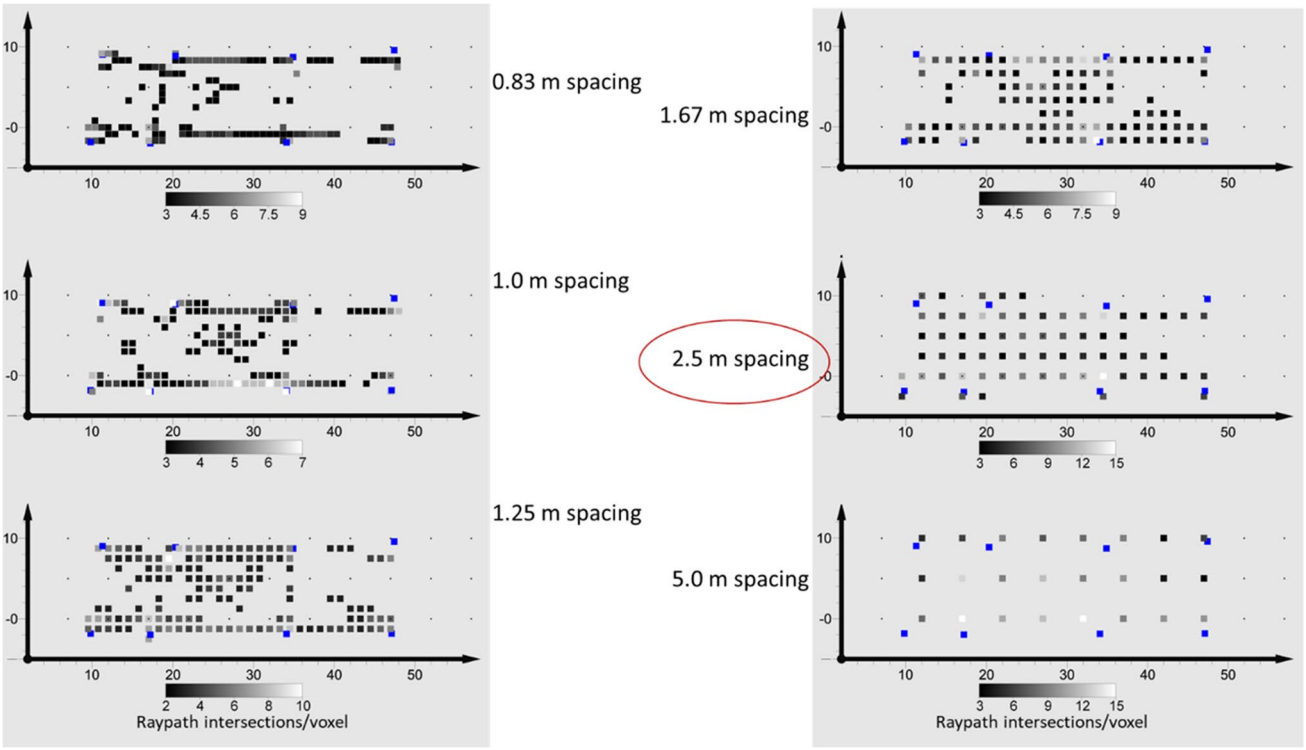

Fig. 3 Voxel spacings ranging from 0.83 to 5 m and also voxels that have at least three rays passing through them (legend for each plot shows the number of rays passing through each voxel)

rays passing through each voxel). Voxel coverage extends in three dimensions, but because the source points and receiver locations were at approximately the same elevation, the plotted results represent a horizontal cross-section through the pillar. Figure 3 shows that with relatively close spacing (from 0.83 to 1.67 m per voxel) not all of the voxels in the interior of the pillar have rays passing through them. A spacing of 2.5 m between voxels was selected as most of the voxels in the interior of the pillar have rays passing through them. A spacing of 5 m between voxels would also be reasonable, but the smaller spacing was preferred for this study.

The tomography calculation for each time period used its median velocity as the initial uniform background velocity and one iteration assuming straight raypaths was conducted in order to determine an initial velocity distribution. The SIRT method is iterative and approaches the solution gradually; using this method, it is necessary to select the iteration which provides the best-fit solution. Following the first iteration, an additional 25 iterations were completed using the Fast Marching Method to approximate the refracted raypaths. The summed root mean square (RMS) difference between the measured and calculated travel times for each iteration was plotted. The best-fit solution was selected as the iteration nearest the elbow of the curve. Iterations prior to the elbow underfit the data and iterations beyond the elbow overfit the data such that the calculated velocity distribution uses velocities which may exceed those that are physically possible. The RMS differences between measured and calculated travel times for the four time periods were 7.7e-5, 6.2e-5, 3.5e-5, and 1.38e-4 s, respectively. The results from the best-fit solution were gridded with Inverse Distance to first power at 1-m spacings and a 7.5-m search radius.

4 Data Analysis

Prior to discussing the specific results as shown in the tomograms, it is important to understand the overall change in velocity observed throughout the pillar, as well as the raypath coverage within the pillar. The resulting tomograms may then be compared to the measured convergence [23] and the relative expected stress change due to the longwall face approaching the pillar. The relative size and shape of the velocity distribution can be compared to the expected size and shape of the stress distribution as well.

4.1 Overall Velocity Change

The mean velocity of all P-waves traversing the pillar on a specific date is an indicator of the overall, general stress within the pillar at that time. Laboratory studies have shown that there is a somewhat monotonic relationship

between stress and P-wave velocity [24, 25]. In many of the studies the P-wave velocity increases with increasing stress, until the stress within the sample nears its ultimate strength, at which time microfractures develop within the sample resulting in a reduced P-wave velocity. Another way to understand the relationship between P-wave velocity and induced stress is through the equation relating the two. Equation 1 shows that the P-wave velocity (v_P) within an elastic media can be calculated as a function of bulk modulus (K), shear modulus (μ) and density (ρ):

$$v_P = \sqrt{\left[\frac{K + \frac{4}{3}\mu}{\rho}\right]} \quad (1)$$

The P-wave velocity is proportional to the bulk and shear moduli, and as the pillar is loaded and the material becomes stiffer, due to closure of microfractures within it, and the P-wave travels with a greater velocity.

For this study, the mean velocity within the pillar increased from 2532 m/s on Oct 18, to 2618 m/s on Nov 18, to 2899 m/s on Dec 18, and then dropped to 2404 m/s on Dec 27. This relative increase in velocity is similar to prior work in laboratory coal specimens [26], and as would be expected, these results are parallel to those shown in Fig. 2. The broad conclusion that can be drawn solely from the overall mean velocity is that the pillar appears to have reached its ultimate load sometime between Nov 18 and Dec 27; the peak velocity occurs sometime between those two dates. Dec 18 has the highest recorded mean velocity of the four study periods but that date, but it cannot be stated definitively that the peak velocity occurred precisely on this date.

4.2 Raypath Coverage

Figure 3, in the illustration with 2.5 m spacing, shows the number of raypaths which traverse each voxel within the pillar for each of the four dates. It is necessary to understand the raypath coverage so that the relative levels of confidence of the velocities within the pillar can be understood. The interior of the pillar has between 5 and 15 rays per voxel, indicating good raypath coverage and a relatively high level of confidence in the results. However, there are differing levels of raypath coverage through the ends of the pillar and there are fewer raypaths through the interior of the outby portion of the pillar than for the inby portion of the pillar, so there is lower confidence in the results seen in the outby section of the pillar (note that 'inby' refers to the direction that is away from the mine portal and toward the working face, whereas 'outby' refers to the direction that is away from the working face and toward the mine portal).

4.3 Tomograms

The resulting tomograms for the four face locations are shown in Fig. 4. In this figure, the beltway is at the bottom of the figure and the travelway is to the top, black squares on the plots are source locations along pillar ribs, the horizontal cross sections shown are at an elevation between the inby and outby source elevations, and the velocity scales vary. As shown in Fig. 4, the distribution of the velocity changes

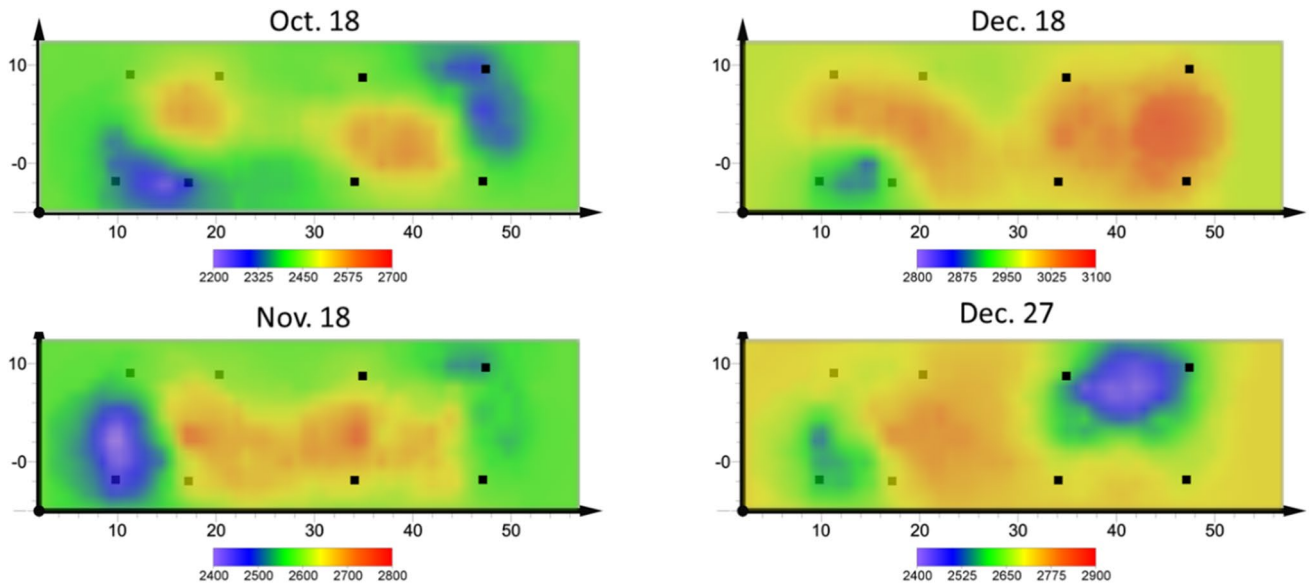

Fig. 4 P-wave velocity tomograms for four time periods, geophones shown as black markers. Axis units are meters; velocity units are meter per second (m/s

from two high-velocity peaks on Oct 18, to a broader high-velocity 'ridge' on Nov 18, to a fairly uniform high velocity across the entire pillar on Dec 18. Finally, on Dec 27, there is a single high-velocity peak within the inby portion of the pillar and a low-velocity in the outby portion of the pillar. There is a consistent low-velocity zone on all four tomograms for the beltway rib on the inby end of the pillar; one possible explanation for this observation is that this portion of the pillar yielded as a result of a local geologic anomaly or possibly an anomalous mining practice. Similarly, there is a low-velocity zone on three of the dates for the travelway rib on the outby end of the pillar (observed Oct 18, Nov 18, and Dec 27). The maximum velocity within the tomogram rises from 2580 m/s on Oct 18, to 2775 m/s on Nov 18, to 3,369 m/s on Dec 18 and then to 2798 m/s on Dec 27. This variation is slightly higher than the observed mean velocity for all of the raypaths for each date through the pillar, as shown in Fig. 2. The highest velocities were observed in the core of the pillar, toward the inby end. In a previous study applying seismic refraction tomography through the floor under a longwall yield pillar, Freidel et al. [16] also observed the highest velocities in the core of the pillar, toward the inby end.

5 Results

5.1 Comparison to Previous Studies

Stress measurements within the pillar were not acquired in this study, but the tomographic results may be compared to previously published stress measurements in similar pillars. Prior research under similar conditions at another two-entry, longwall mine in the western United States has related onset of forward abutment stresses to the ratio of distance from face to overburden thickness using borehole pressure cells in pillars [27]. Although similar pillars exhibited differing responses, the consensus observation was that peak pressure within the pillar, which was followed by yielding, occurred when the ratio of face distance to depth was reduced to 20%, that is, when the face was located at a distance to the pillar 20% of the overburden thickness. In the current study, the overburden thickness at the pillar was approximately 400 m, and the face locations evaluated in this study were 678 m, 320 m, 114 m, and 41 m away from the inby end of the pillar, resulting in face locations that were 170%, 80%, 28%, and 10% of the overburden thickness from the pillar. The behavior shown in the current study is similar to that observed by the prior study. The peak velocity, indicating peak loading, occurs at approximately the same ratio of face distance to depth, less than 28% in the current study versus 20% in the prior study.

5.2 Comparison to Geotechnical Monitoring (Convergence)

As a pillar undergoes increased loading it would generally be expected that there would be an associated increase in roof-to-floor convergence and that the inby end of the pillar may show more convergence than the outby end; however, geologic variation can also affect convergence. Throughout this study, convergence measurements were taken at points around the pillar (locations are shown in Fig. 1), and these measurements were compared to the results of the tomograms. Table 2 shows the measured convergence on the four dates included in this study. The convergence increased for all points as the face drew nearer, the inby measurement points (B04 and T04) had greater convergence than the outby points, and the convergence increased monotonically from outby to inby points through all time periods. In summary, convergence was highest at the pillar locations closest to the longwall face and convergence increased across the entire pillar as the face advanced.

Overall, the convergence monitoring data appear supportive of the tomographic results. In the tomography study, the mean velocity increased across the entire pillar for the first three dates, indicating increasing load, and then decreased from the third to fourth date, indicating post-peak behavior. This observation is compatible with the observed convergence measurements. The greatest amount of convergence occurred between the third and fourth dates. On average, only 1.8 mm of convergence was measured between Oct 18 and Dec 18, whereas an average of 4.9 mm of convergence was measured for the eight points between Dec 18 and Dec 27. As a more localized comparison, convergence station B04, located on inby end of the pillar along the beltway, had the most roof-to-floor convergence, and this region also showed a low-velocity zone in the tomographic results, which perhaps indicates that this location was relatively weak, or prematurely yielded. It should be noted, however,

Table 2 Measured convergence at the four dates for which tomograms were generated

		Distance to Face (m)			
		678	320	114	41
		Convergence (mm)			
Travelway	T4	2.1	3.1	6.1	12.0
	T3	0.8	1.2	3.0	5.3
	T2	0.6	1.1	2.2	3.8
	T1	0.5	0.8	1.5	2.0
Beltway	B4	4.2	6.0	11.6	19.1
	B3	1.0	1.8	4.2	7.5
	B2	0.8	1.2	2.7	5.5
	B1	0.3	0.7	1.4	3.1

that the tomographic results also show a low-velocity zone near convergence station T02, but the measured convergence at T02 was not larger than adjacent stations.

5.3 3 Comparison to Theory

Pillar strength and behavior is not only a function of coal strength and pillar shape, but also of constraint imposed by material properties of the roof and floor interfaces [28]. The stress redistribution within a pillar due to the nearing of the longwall face with a stiff overburden typically transfers stresses over a greater distance than in seams with a relatively less stiff overburden [29]. Because the floor and roof strata at the study site were of moderate strength, primarily a shaly sandstone with occasional mudstone lenses, it would be expected that the stress within the pillar would redistribute within the typical pattern expected from prior theories, as well as numerical modeling results.

The distribution of the velocity within the pillar aligns fairly well with the proposed theoretical stress distribution by Wilson [6] and Wagner [9] and others. The theoretical stress redistribution within a pillar under increasing load is stress that is initially evenly distributed to the perimeter of the pillar, and then, as the perimeter fails, stress migrates toward the confined core and the level of stress within the confined core increases. In other words, as load on the pillar increases and portions of the pillar fail, then the remaining, intact portions of the pillar accept an increasingly higher load. This redistribution agrees with that shown in Fig. 4 where the velocity increases in magnitude and migrates toward the interior of the pillar during the first three time periods, then from the third to the fourth time period the magnitude of the velocity decreases, and it could be interpreted that by the fourth time period, a portion of the pillar has failed and potentially load has transferred to surrounding pillars.

5.4 Comparison to Numerical Models

Advances made in computing capabilities have led the development and use of numerical tools to simulate stress-induced yielding and damage process of rocks and rock masses, including the boundary element method, the finite difference method, and the finite element method [30]. As described by Larson and Whyatt [31], ALPS, MULSIM/NL, LaModel, and FLAC are stress analysis software tools used for evaluating mine layout design. Numerical models are able to provide useful results for an extreme range of mining conditions, including changing stress due to longwall face advance [29]. Carefully implemented finite element analysis based on first principles of mechanics is well-suited for rational design of safe underground entries and crosscuts, barrier pillars, and bleeder entries [32]. Monitoring, including convergence, can be important for calibration of numerical models, including finite element models [33].

A whole-mine finite element model was generated to evaluate changes in stress in the test pillar related to face advance. The numerical model used a special adaptation of the finite element method called Dual Node-Dual Mesh. This adaptation has been used in previous studies to effectively model whole-mine history, current, and future mining [34]. Input data for the finite element model included digital topography, mine plans, a stratigraphic column with strata thicknesses and depths, strata properties including elastic moduli and strengths, and joint set geometry. In this regard, element properties were assigned statistically for greater realism in accordance with spatial variability. The output results include displacements induced by panel mining, distribution of stress, and distribution of element safety factors. The element safety factors were calculated based upon a non-linear, anisotropic form of the Drucker-Prager criterion; additional modeling details and analysis are summarized by Pariseau et al. [32].

Figure 5 illustrates the safety factor distribution within the pillar at four percentages of panel face advance, 55%, 75%, 87%, and 91%, which correspond closely to the panel advance on each of the four dates, Oct 18, Nov 18, Dec 18, and Dec 27. Some features of the numerical models and the velocities from tomography are comparable. Consistently, the numerical model shows the lowest safety factors in the beltway near the inby edge of the pillar; in all of the tomographic results, there is a low velocity zone near this region. Safety factors in the interior of the pillar are generally high, greater than 2.7, but show the largest decrease from 87 to 91% panel mined. This observation appears to support the decrease in maximum velocity from Dec 18 to Dec 27.

6 Summary

The results obtained in the current study agree to a large extent with the expected distribution and relative magnitude of induced stress, as presented in prior studies. P-wave travel time tomography provides a method to examine the redistribution of stress throughout a specified volume of a rock-mass, complementing other methods such as point-location measurements and numerical modeling. The information provided by the tomograms can be useful to confirm that an optimal pillar design is being used – a design that maintains safety and does not sacrifice productivity.

7 Conclusions

Active seismic tomography was conducted on a yield pillar in a longwall mine in the western United States. Although computed tomography has been relied upon in the medical

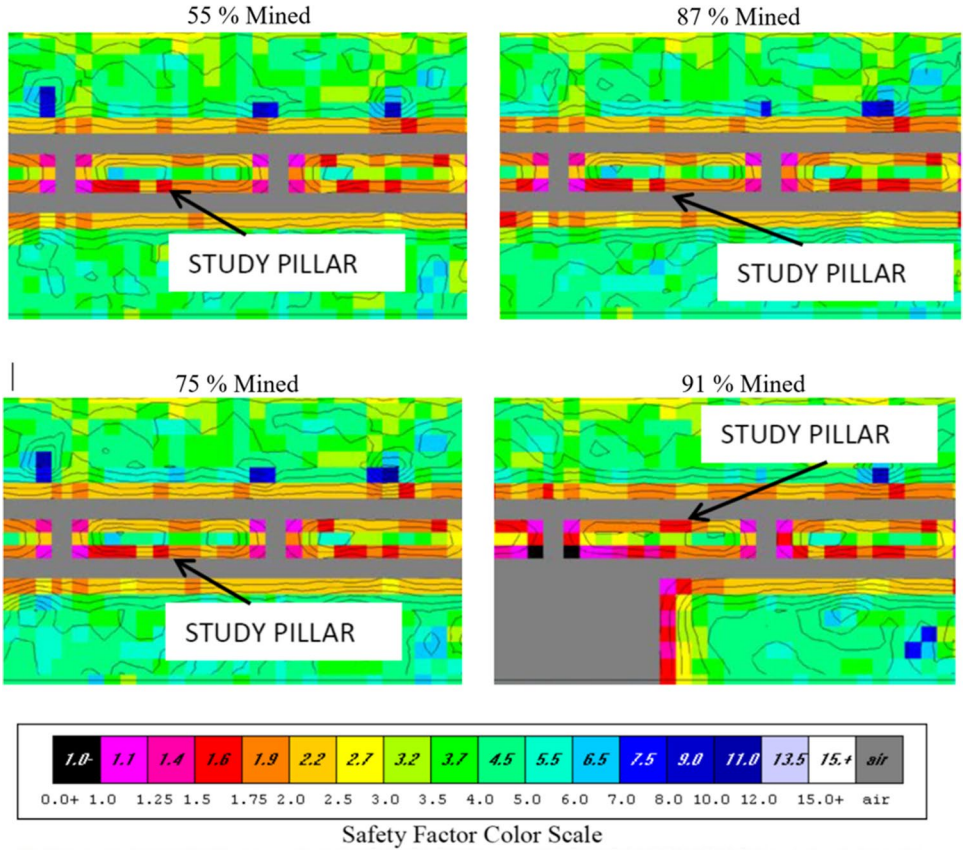

Fig. 5 Safety factor distribution from finite element analysis of the pillar and surrounding region for four stages of panel advance which correspond closely to the dates included in the tomographic analysis

field for decades, and has the ability to provide information about conditions throughout a rockmass, it is still not a common method in the mining industry. This study provides an opportunity to compare results from active seismic tomography in a well-defined, unambiguous study to those from current theory, numerical modeling, and point measurements.

Data for the tomograms were collected when the longwall face was 678 m, 320 m, 114 m, and 41 m inby the pillar, resulting in increased loading on the pillar. The purpose of the study was to determine whether active seismic tomography would allow a measurement of the pillar volume that could be compared to traditional pillar design understanding from theory, numerical modeling, and point-location measurements. With increased knowledge of pillar load distribution, optimal pillar dimensions can be selected such that both safety and efficient extraction of a resource are allowed.

The tomography results generally agree with those proposed by theory, convergence measurements, and numerical models. This observation provides two conclusions: (1) The agreement of the methods provides validation for the theorized stress redistribution, and (2) this study provides further evidence that tomography can indicate the redistribution of induced stress within a mined rockmass and tomography is another tool available to ensure that mining is conducted safely and efficiently. We can also conclude that at the mine in the study, for the loading conditions, the pillar size was within acceptable bounds, the pillar did not fail prematurely; however, it was not over-designed and thus inefficient.

In addition to the data from the active seismic source, microseismic data were collected continually during this experiment. Future research can include using the microseismic events as sources for conducting passive seismic tomography. The advantages of passive seismic tomography is that a more continuous set of data are typically available, and there is potential for greater resolution within the tomograms if a sufficient number of microseismic events are recorded.

Acknowledgements The significant support of the mine operator and mine personnel is thankfully acknowledged.

Funding Funding for this research was provided by the National Institute for Occupational Health and Safety (NIOSH). The conclusions of this work are those of the authors and do not necessarily represent the opinions or policies of NIOSH.

Declarations

Conflict of interest The authors declare no competing interests.

References

1. Holland, CT (1964) The strength of coal in mine pillars. In: Proceeding of the 6th US symposium on rock mechanics. ARMA, Rolla, MO, pp 450–466
2. Obert L, Duvall WI (1967) Rock mechanics and the design of structures in rock. J Wiley, New York, p 650
3. Salamon MDG, Munro AH (1967) A study of the strength of coal pillars. J of South Afr Inst Min Metall 68(2):55–67
4. Bieniawski ZT (1968) In situ strength and deformation characteristics of coal. Eng Geol 2(5):325–340
5. Wilson AH (1972) An hypothesis concerning pillar stability. Min Eng (London) 131(141):409–417
6. Wilson AH (1981) Stress and stability in coal ribsides and pillars. In: Proceedings of the first international conference on ground control in mining. West Virginia University, Morgantown, WV, pp 1–12
7. Mark C (2000) State-of-the-art in coal pillar design. Trans-Soc Min Metal Explor Incorp 308:123–128
8. Wagner H (1974) Determination of complete load deformation characteristics of coal pillars. In: 3rd Congress International Society Rock Mechanics. US National Academy of Science, Denver, CO, pp 1076–1081
9. Wagner H (1980) Pillar design in coal mines. J of South Afr Inst Min Metall 801(1):37–45
10. Koehler JR, DeMarco MJ, Marshall RJ, Fielder J (1996) Performance evaluation of a cable bolted yield-abutment gate road system at the Crandall Canyon No. 1 Mine, Genwall Resources, Inc., Huntington, Utah. In: Proceedings of the 15th international conference on ground control in mining. Colorado School of Mines, Golden, CO, pp 77–95
11. Esterhuizen E, Mark C, Murphy MM (2010) Numerical model calibration for simulating coal pillars, gob and overburden response. Proceeding of the 29th international conference on ground control in mining. West Virginia University, Morgantown, WV, pp 46–57
12. Mark C (1987) Analysis of longwall pillar stability. Dissertation, Pennsylvania State University
13. Cormack AM (1973) Reconstruction of densities from their projections, with applications in radiological physics. Phys Med Biol 18(2):195–207
14. Houndfield GN (1973) Computerized transverse axial scanning (tomography). 1. Description of system. Br J Radiol 46(552):1016–1022
15. Westman EC (1993) Characterization of structural integrity and stress state via seismic methods: a case study. In: Peng SS (ed) Proceedings, twelfth international conference on ground control in mining. West Virginia University, Morgantown, WV, pp 322–327
16. Friedel MJ, Jackson MJ, Williams EM, Olson MS, Westman EC (1996) Tomographic imaging of coal pillar conditions: observations and implications. Int J Rock Mech Min Sci Geomech Abstr 33(3):279–290
17. Goldstein P, Snoke A (2005) SAC availability for the IRIS community. Incorporated Research Institutions for Seismology Newsletter 7(UCRL-JRNL-211140)
18. Goldstein P, Dodge D, Firpo M, Minner L, Lee WH, Kanamori H, Jennings PC, Kisslinger C (2003) SAC2000: Signal processing and analysis tools for seismologists and engineers. IASPEI Int Handb Earthq Eng Seismol 81:1613–1620
19. Kroon DJ (2020) Accurate Fast Marching. MATLAB Central File Exchange. https://www.mathworks.com/matlabcentral/fileexchange/24531-accurate-fast-marching. Accessed 15 May 2021
20. Coons DJ (2020) Seismic analysis to assess velocity changes in a yield pillar. University of Utah, Thesis
21. Sethian JA (1996) A fast marching level set method for monotonically advancing fronts. Proc Natl Acad Sci 93(4):1591–1595
22. Rawlinson N, Spakman W (2016) On the use of sensitivity tests in seismic tomography. Geophys J Int 205(2):1221–1243
23. Coons DJ, McCarter MK, Wempen JM, Simmons BS (2020) Experimental evaluation of a two-entry gate-road yield pillar: convergence monitoring and physical properties. Min Metall Explor 37:701–708
24. Terry NB (1959) Dependence of elastic behavior of coal on microcrack structure. Fuel 3:125–146
25. Seya K, Suzuki I, Fujiwara H (1979) The change in ultrasonic wave velocities in triaxially stressed brittle rock. J Phys Earth 27:409–421
26. Shea-Albin VR, Hanson DR, Gerlick RE (1991) Elastic wave velocity and attenuation as used to define phases of loading and failure in coal. No 9355. Bureau of Mines, US Department of the Interior, p 43
27. Haramy KY, Kneisley RO (1990) Yield pillars for stress control in longwall mines — case study. Intl J Min Geol Eng 8(4):287–304
28. Babcock C, Morgan T, Haramy K (1981) Review of pillar design equations including the effect of constraint. In: Proceedings of the first international conference on ground control in mining. West Virginia University, Morgantown, WV, pp 23–34
29. Esterhuizen GS, Gearhart DF, Klemetti T, Dougherty H, van Dyke M (2018) Analysis of gateroad stability at two longwall mines based on field monitoring results and numerical model analysis. Inter J Min Sci Technol 29(1):35–43
30. Li X, Kim E, Walton G (2019) A study of rock pillar behavior in laboratory and in-situ scales using combined finite-discrete element method models. Int J Rock Mech Min Sci 118:21–32
31. Larson MK, Whyatt JK (2009) Deep coal longwall panel design for strong strata: the influence of software choice on results. In Proceedings of the international workshop on numerical modeling for underground mine excavation design, pp 75–89
32. Pariseau WG, McCarter MK, Wempen JM (2019) Comparison of closure measurements with finite element model results in an underground coal mine in central Utah. Inter J Min Sci Technol 29(1):9–15
33. Stricklin KG (2013) Roof control plan approval and review procedures. Mine Safety and Health Administration Handbook Number PH13, 4.
34. Pariseau, WG (2017) Comparison of Underground Coal and Trona Mine Seismicity. Society of Mining, Metallurgy and Exploration Annual Meeting, Preprint 17–027, SME, Denver, CO.